



Raster approach to modelling the failure of arbitrarily inclined interfaces with structured meshes

Simone Falco^{1,2} · Nicholas Fogell² · Lorenzo Iannucci² · Nik Petrinic¹ · Daniel Eakins¹

Received: 5 November 2023 / Accepted: 5 February 2024
© The Author(s) 2024

Abstract

This paper presents an approach to evaluate the failure of arbitrarily inclined interfaces using FE models with structured spatial discretization, providing accurate prediction of crack propagation along paths known a priori that are not constrained to the element boundaries. The combination of algorithms for the generation of structured discretization of representative polycrystalline microstructures with novel cohesive element formulations allow modelling the failure of complex topologies along rasterised boundaries, with noticeably higher computational efficiency and comparable accuracy. Two formulations of raster cohesive elements are presented, adopting either elastic-brittle or Tvergaard–Hutchinson traction separation laws. The formulations proposed are first validated comparing the failure of the interface within bi-crystal structures discretised using hexahedral elements either within a structured mesh (i.e. with rasterised boundaries) or an unstructured mesh (i.e. with planar boundary). Subsequently, the effectiveness of the formulations is demonstrated comparing the inter-granular crack propagation within complex polycrystalline microstructures. The behaviour of the novel cohesive element formulation in structured meshes consisting of regular hexahedral elements is in excellent agreement with the deformation and failure of classic cohesive element formulations placed along the planar boundaries of unstructured meshes consisting of tetrahedral elements. The higher computational cost of the raster cohesive elements is more than compensated by the increase in computational efficiency of structured meshes when compared to unstructured meshes, leading to a reduction of the simulation time of up to over 200 times for the simulations presented in the paper, thus allowing the simulation of large domains.

Keywords Inter-granular crack propagation · Raster discretization · Structured mesh · Cohesive element formulation · Traction separation law

1 Introduction

Modelling the failure of materials due to brittle crack propagation is a common aim in structural mechanics that still presents significant numerical challenges [1].

One of the first developed, and arguably simplest approaches to simulate the initiation and propagation of cracks within a solid structure is the combination of element erosion techniques and the classic Finite Element Method (FEM). As the crude removal of elements that reach certain failure criteria leads to non-physical loss of mass in the model, several mod-

ifications of the method have been presented to account for the correct energy dissipation [2].

Despite the corrections, however, the tridimensionality of the removed elements creates a void in the model, blunting the crack tip and limiting the accuracy of the approach. Several methods have been developed to introduce sharp (i.e. 2D) discontinuities in tridimensional models along arbitrary directions, either as modifications of the classic FEM (e.g. XFEM [3]), as well as meshless methods (e.g. SPH [4], RKPM [5]), all proving effective to reproduce failure due to crack propagation along arbitrary paths.

However, for problems in which the potential crack paths are known *a-priori*, (e.g. grain boundaries of some brittle polycrystalline microstructures, interfaces in composite materials) the classic FEM approach is still arguably the most commonly used method owing to its combination of robustness and computational efficiency [6]. Within the FEM method, the fracture process along potential crack paths

✉ Simone Falco
simone.falco@eng.ox.ac.uk

¹ Department of Engineering Science, University of Oxford, Parks Road, Oxford, UK

² Department of Aeronautics, Imperial College London, Exhibition Road, London, UK

known *a-priori* is described by a cohesive zone model (CZM) with a phenomenological traction-separation law (TSL) governing the interface behaviour [7]. The most common implementation of the CZM approach is the use of cohesive elements, with crack opening represented as displacement jumps within the finite element.

The original implementation of the cohesive element method is the so-called *intrinsic* approach, which imposes an initially elastic response followed by a stiffness reduction (i.e. softening) [8, 9]. A well-known limitation of the intrinsic approach is the introduction of an *artificial compliance* in the model, due to the initial elastic slope of the TSL. The effect can be limited by increasing the initial stiffness of the cohesive element, which comes at the cost of a reduction in the stable time step for the simulation [10].

An alternative implementation, pioneered by Camacho and Ortiz [11] and Ortiz and Pandolfi [12] is based on the insertion of cohesive elements during the simulation when certain bulk criteria are satisfied. This so-called *extrinsic* approach effectively imposes an initially rigid TSL, thus avoiding artificial compliance issues prior to fracture. However, the insertion of cohesive elements *on-the-fly* presents its challenges due to the complexity of the required mesh topology modifications (i.e. node splitting and redefinition of element connectivity) [13].

Both cohesive element approaches require the potential crack paths to lie along element boundaries, introducing constraints on the spatial discretisation that prevent the use of computationally efficient structured meshes. The flexibility afforded by a mesh of tetrahedral elements limits the presence of small and/or distorted elements in the discretisation of complex geometries, however the linear (i.e. four nodes) formulation exhibits *locking* behaviour under certain loading conditions, causing significant loss of accuracy [14]. Several approaches have been developed to prevent locking in tetrahedral elements (e.g. increasing the order of the polynomial shape functions), generally leading to a significant increase in the computational cost of the simulation. Conversely, hexahedral elements guarantee high accuracy and low computational cost, but introduce significant complexity to the discretization of irregular domains. There are several algorithms that allow the discretization of arbitrary geometries into hexahedral elements (e.g. Hypermesh [15], CUBIT [16]), but they still require a degree of user effort to mesh highly irregular shapes, which makes them unsuitable for automated modelling of complex geometries such as polycrystalline microstructures. Additionally, the use of unstructured hexahedral meshes is still susceptible to the presence of distorted elements, which affects the overall computational cost and accuracy of the simulation. In general, for complex structures with many potential crack paths—like the polycrystalline microstructures prone to inter-granular crack propagation presented in this paper—highly irregular

geometries can lead to a trade off between the quality of the elements and the computational cost of the simulation, making the accurate modelling of the failure of even relatively small domains unfeasible.

Structured meshes consisting of hexahedral elements, on the other hand, offer the ideal combination of high accuracy and low computational cost, and are often used for large models and/or complex simulations [17, 18]. For heterogeneous structures, however, the numerical advantages come at the expense of an approximate discretisation of boundaries, which hinder the use of the classic formulation of the CZM approach, as the element boundaries do not lay on the possible crack paths.

The presence of voxellated boundaries is also common in microscopy imaging of heterogeneous domains such as polycrystalline microstructures, due to the limits of imaging resolution. The correction of voxellated boundaries—caused by the pixel-based nature of digital images—into a smooth conformal surface mesh is a frequent issue in the elaboration of images [19].

The development of interface formulations which can accurately predict the behaviour of voxellated boundaries is key to exploiting the high computational efficiency of regular hexahedral elements to simulate crack propagation within topologically complex structures, and possibly to reduce the need for elaborate processing of digital images into conformal meshes. A reduction in computational cost, compared to models discretised with unstructured meshes, facilitates the use of raster polycrystalline RVEs in multiscale simulation frameworks. Such multiscale frameworks allow for completion of large parametric studies for the statistical homogenisation of the results at the microscale [20].

This paper presents a novel approach to the modelling of the failure of voxellated structures by implementing cohesive laws capable of reproducing inter-granular crack propagation along the grain boundaries of a polycrystalline structure. First a method for the generation of statistically representative models of polycrystalline microstructures is presented, highlighting its ability to evaluate and store the orientation of each grain boundary in the domain before discretising the geometry into a rasterised hexahedral mesh. Then the adaptation of the CZM formulation to raster interfaces, based on the transformation of the stress state in the cohesive elements along the voxellated boundary into shear and normal stress components along the original planar interface, is presented. The adaptation of two cohesive laws (elastic-brittle and Tvergaard–Hutchinson) is illustrated in detail, and the novel formulations are validated against the corresponding TSL for planar interfaces, proving the ability of the method presented to combine robust and computationally efficient structured hexahedral meshes with accurate prediction of crack propagation along arbitrarily oriented planar boundaries.

2 Generation of FE models

Preparation of the FEM models presented in this paper relies on the combination of an algorithm for the generation of representative polycrystalline microstructures and a raster discretisation approach that can create a structured mesh of the microstructure and insert cohesive elements along the raster boundary. The information on the original inclination of the planar interface is stored in each of the newly inserted zero-thickness elements in the form of the normal unit vector components in the global coordinate system. This is used by the material model to transform the stress and deformation state from the local element coordinate system into that of the original interface plane.

2.1 Microstructure generation

The geometries presented in this paper are created using the VorTeX package [21] to generate representative models of polycrystalline microstructures. The algorithms are based on the Laguerre–Voronoi tessellation technique to divide the entire three-dimensional space into polyhedral cells. Specifically, given an arbitrary set of nuclei, the cells consist of the points closer, in terms of power distance, to the corresponding nucleus than to any other nuclei in the domain. Analytically, the Laguerre–Voronoi tessellation can be expressed as

$$\{R_{P_i}\} = \{x \in \mathbb{R}^3 : \text{pow}(\mathbf{x}, (\mathbf{P}_i, \omega_i)) \leq \text{pow}(\mathbf{x}, (\mathbf{P}_j, \omega_j))\} \\ \forall j = 1, 2, \dots, N : j \neq i \quad (1)$$

where \mathbf{P}_j is the position of the j -th nucleus, $\{R_{P_i}\}$ the locus of points forming the cell associated to the nucleus \mathbf{P}_i , \mathbf{x} is the position of a generic point in the three-dimensional space \mathbb{R}^3 , and ω indicates the weight of each nucleus.

The power distance between a generic point x and a nucleus P_i is defined as the difference between Eulerian distance ($\|\mathbf{P}_i - \mathbf{x}\|$) and the weight of the nucleus ω_i :

$$\text{pow}(\mathbf{x}, (\mathbf{P}_i, \omega_i)) = \|\mathbf{P}_i - \mathbf{x}\|^2 - \omega_i \quad (2)$$

The use of power distance instead of the classic Eulerian distance offers enhanced control over the cell size distribution, thus providing the capability to increase the representativeness of the models generated. The complexity of the formulation due to the introduction of the concept of *weight* of a nucleus, and the level of representativeness achievable are discussed in detail in [22].

As a direct consequence of Eq. (1), each cell generated with Laguerre–Voronoi tessellation is a polyhedral domain bounded by planar polygonal faces, and univocally defined as the convex hull of its vertices. The planar faces also define the boundary between cells, allowing the shape and orientation of the interfaces along which failure can propagate to be

easily identified, as can be seen in the example polycrystalline geometry presented in Fig. 1a.

The orientation of each interface in the domain, which is key to the novel raster cohesive element approach presented herein, is calculated from the coordinates of the vertices. The information is then used to assign the correct properties to the cohesive elements introduced along the grain boundaries of the raster mesh, as presented in the next section.

2.2 Raster discretisation

The discretisation of the domain is performed by superimposing a regular three-dimensional grid on the tessellation geometry. To increase the computational efficiency of the discretisation algorithm, a two-step method has been implemented: first a fast screening of the position of the centre of each hexahedral element against the bounding box of each cell is performed, followed by a more accurate assessment of the position of each element with respect to the actual boundaries of each cell.

The use of bounding boxes for each cell, defined by the minimum and maximum coordinates of the cell vertices along global directions x , y , and z allows the fast identification of the subset of cells potentially containing the element. In case multiple cells are identified for a single element, the actual convex hull containing the centre of the element is calculated. Finally, all the elements whose centres fall into the same cell are grouped into a part.

The two-step rasterisation method allows the discretisation of complex geometries into a structured hexahedral mesh with minimal computational cost, providing FEM models of polycrystalline topologies of the type presented in Fig. 1b.

To model the grain boundaries, zero-thickness cohesive elements are added between neighbouring bulk elements belonging to different parts, as shown in Fig. 1c. The voxelation of the interfaces obscures the actual slope of the boundaries, which is fundamental to correctly calculating the stress state in the cohesive elements. The information is gathered from the tessellation by extracting the list of faces shared by neighbouring grains. The slope of each grain boundary—expressed in terms of the components of the normal unit vector—is then calculated and stored as an *interface property*. By assigning each element to the corresponding boundary, the cohesive law algorithm has access to the slope components required to correctly evaluate the stress state in the raster element. The approach developed requires the definition of the cohesive properties for each interface, thus providing full control to the user on the strength and toughness of the boundaries.

The formulation and implementation of the two cohesive material models implemented is presented in the next section, followed by the validation of the approach against analytical

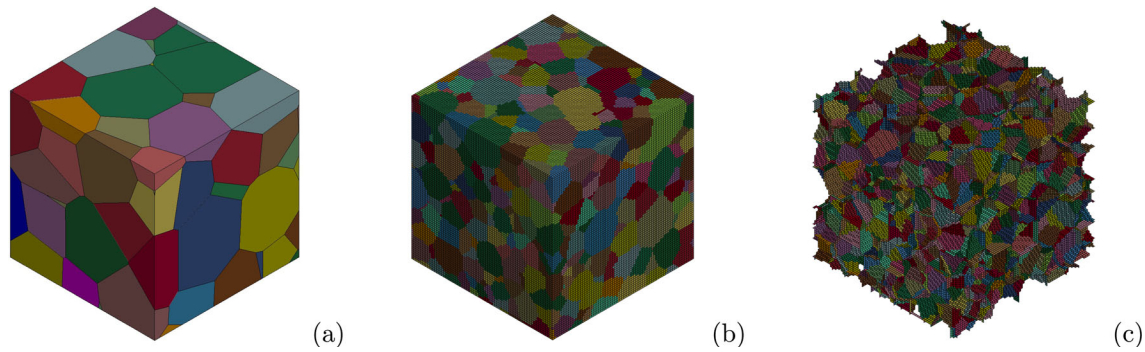


Fig. 1 Visualisation of **a** statistical model of polycrystalline microstructure, **b** rasterised discretisation, and **c** cohesive elements along the grain boundaries

calculations and numerical models with planar interfaces in Sect. 4.

3 Raster cohesive elements formulation

The formulation of the raster cohesive elements is based on the rotation of the stress tensors evaluated on the raster interfaces during the numerical simulation, onto the normal and tangential directions of the original inclined interface.

To track the transformation of the stress components from the raster elements to the original inclined interface, three coordinates systems are defined: *element local* $[\xi\eta\zeta]$, *global* $[xyz]$, and *planar local* $[123]$, as graphically represented in Fig. 2.

The *element local* coordinates are defined consistently with LS-Dyna convention: the first two coordinates (ξ and η) are in the plane of the cohesive element, and the third coordinate (ζ) is normal to it. The *global* coordinate system, is instead consistent for the whole model. Its axes are parallel to the axes of the *element local* coordinate system but independent of the orientation of the single cohesive element. Finally, the *planar local* coordinate system is defined per each interface, with the first two directions (1 and 2) lying on the plane of the interface, and the third direction (3) perpendicular to it.

The rotation of stresses (or jump) from *element local* to *global* coordinates is relatively straightforward, as it is performed by rotating the axis by multiples of $\pi/2$ to align all quantities in the $[xyz]$ directions. The rotation from *global* to *planar local* coordinates, instead, is based on the direction cosines of the planar interface stored during the raster discretisation of the domain. Naming N_x , N_y , and N_z the direction cosines of a generic interface with respect to the global directions x , y , and z , respectively, the rotation matrix \mathbf{N} can be expressed as:

$$\mathbf{N} = \begin{bmatrix} N_y & N_z & N_x \\ N_z & N_x & N_y \\ N_x & N_y & N_z \end{bmatrix} \quad (3)$$

Finally, to account for the difference in area between the raster elements and the actual planar interface, each raster cohesive element carries only normal force, so that three perpendicular elements are required to fully decompose the forces on a general planar interface. The appropriate cosine director is then used to scale the area from global $[xyz]$ to the planar local $[123]$ coordinate systems, as expressed in Eq. (7) (for elastic brittle formulation), and Eq. (13) (for the TH formulation), therefore ensuring analytical equivalence between the planar and raster forces.

The approach is used to adapt the two cohesive element formulations presented in this paper: Elastic-Brittle and Tvergaard–Hutchinson cohesive models. Nonetheless, the methodology can be extended to other cohesive element formulations using the transformations presented.

The elastic-brittle cohesive element formulation is one of the simplest models to implement, as it imposes a linear elastic deformation until the sudden and complete failure of the element when either the normal or shear stress reach a user defined threshold value.

The Tvergaard–Hutchinson (hereafter referred to as TH) cohesive law, instead, has a more complex formulation consisting of three regimes: linear elastic, plateau, and softening. The transition between regimes is governed by the separation parameter λ , evaluated from the element deformation along the normal and shear directions.

3.1 Elastic-Brittle cohesive formulation

The elastic-brittle cohesive law is based on MAT_184 of the LS-Dyna material library, a simple cohesive model with perfectly elastic behaviour and sudden failure based on user-defined maximum normal f_n and tangential f_t strength.

The elastic behaviour is described by the relationship between force f and the jump δ in the cohesive element;

$$\begin{Bmatrix} f_1 \\ f_2 \\ f_3 \end{Bmatrix} = \begin{bmatrix} E & 0 & 0 \\ 0 & E & 0 \\ 0 & 0 & E \end{bmatrix} \begin{Bmatrix} \delta_1 \\ \delta_2 \\ \delta_3 \end{Bmatrix}, \quad (4)$$

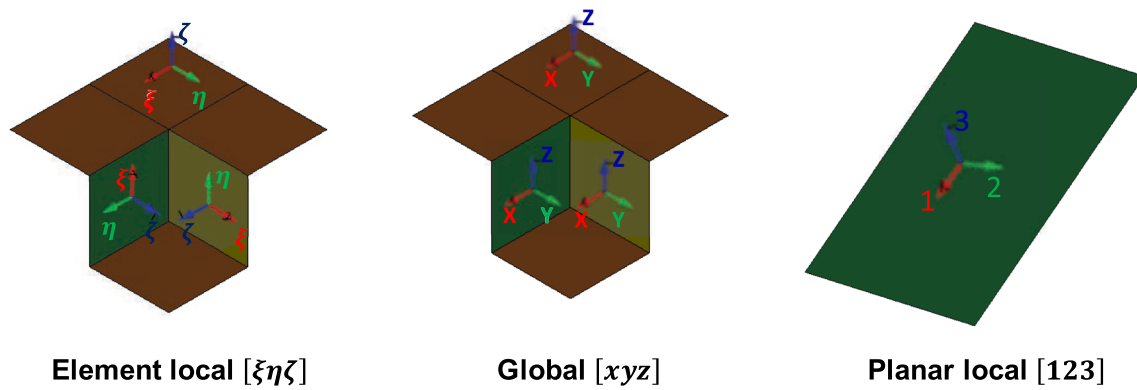


Fig. 2 Coordinate systems defined to track the stress rotation from raster to inclined interfaces

where E is the stiffness of the cohesive element, and the directions [123] are expressed in the planar local coordinate system.

The failure condition is determined by the tangential or normal stress reaching the respective maximum strength, and can be written as;

$$\begin{cases} \sqrt{f_1^2 + f_2^2} = f_t \\ f_3 = f_n \end{cases} \quad (5)$$

To adapt the elastic cohesive formulation to a raster discretisation, the three values of jump (δ_ξ , δ_η , and δ_ζ) are first multiplied by the stiffness to evaluate the local stresses. As the stiffness is imposed to be equal in both tangential and normal directions, the output stress used to evaluate the deformation of the element at the following time step is simply the stress in the direction ζ . To avoid the occurrence of vibrations in the element due to the lack of shear stiffness, a damping term is added to the in-plane stress components, so that the updated stress state in the cohesive element state becomes;

$$\begin{aligned} f_\xi^c &= E\beta\dot{\delta}_\xi \\ f_\eta^c &= E\beta\dot{\delta}_\eta, \\ f_\zeta^c &= E\dot{\delta}_\zeta \end{aligned} \quad (6)$$

where β is a user-defined damping factor, and $\dot{\delta}$ the rate of deformation.

The failure condition is evaluated in parallel to the calculation of the updated stress at the next timestep. This is achieved by first rotating the stress into global coordinates using the direction of the element normal stored during the discretisation process, and then transforming into the stress state that would be experienced by the planar interface, using the relationship defined in Eq. (7). The transformation from xyz to 123 coordinate systems combines the rotation matrix defined in Eq. (3), with the scaling of areas using the direction cosine to assure analytical equivalence between planar and raster stress.

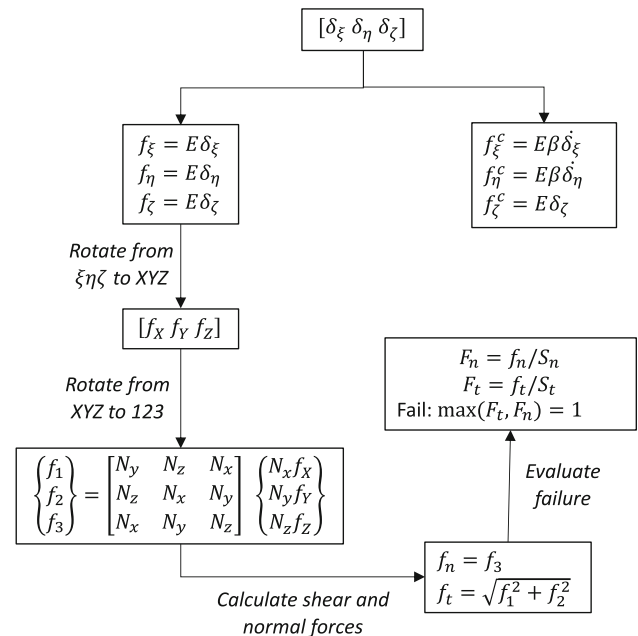


Fig. 3 Flowchart of the raster formulation of elastic-brittle cohesive law

$$\begin{Bmatrix} f_1 \\ f_2 \\ f_3 \end{Bmatrix} = \begin{bmatrix} N_y & N_z & N_x \\ N_z & N_x & N_y \\ N_x & N_y & N_z \end{bmatrix} \begin{Bmatrix} N_x f_x \\ N_y f_y \\ N_z f_z \end{Bmatrix}. \quad (7)$$

The stress state in the local inclined coordinate system is then used to evaluate the failure condition according to Eq. (5), with the failed elements either deleted or imposed to have zero stress, according to user preference.

The algorithm is summarised in the flowchart in Fig. 3, showing the calculation of the updated stress (right branch) and evaluation of the failure condition (left branch).

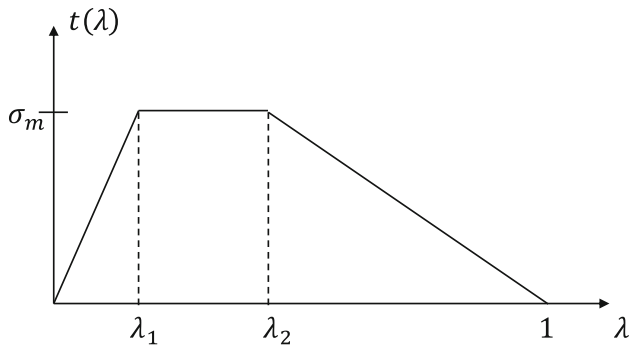


Fig. 4 Graphical representation of the TH cohesive traction law described by Eq. (9)

3.2 Tvergaard Hutchinson cohesive formulation

The simplistic elastic-brittle formulation presented in the previous section has the advantage of requiring very few parameters and a low computational cost both in its classical form and in the raster formulation. However, the abrupt failure of the elements significantly affects the accuracy of the simulation, as the energy released by the failure of an element might trigger the unphysical failure of other elements within the structure. To avoid the occurrence of this type of numerical artefact, a more complex formulation has been adapted to a raster formulation, the Tvergaards-Hutchinson cohesive model [23].

The TH formulation is based on the definition of a dimensionless separation measure λ , which averages the contribution of tangential (δ_1, δ_2) and normal (δ_3) jumps weighted by the user-defined length scales in the tangential (δ_t^c) and normal (δ_n^c) directions,

$$\lambda = \sqrt{\left(\frac{\delta_1}{\delta_t^c}\right)^2 + \left(\frac{\delta_2}{\delta_t^c}\right)^2 + \left(\frac{\langle\delta_3\rangle}{\delta_n^c}\right)^2} \quad (8)$$

where the Macaulay bracket operator $\langle \cdot \rangle$ excludes the negative contribution of δ_3 , therefore preventing unphysical interpenetration along the normal direction of the local planar coordinate system.

The traction across the cohesive element $t(\lambda)$ can be divided into three regimes, determined by the value of λ . The tri-linear stress-deformation law, depicted in Fig. 4, can be described analytically as;

$$t(\lambda) = \begin{cases} \sigma_m \frac{\lambda}{\lambda_1} & \lambda \leq \lambda_1 \\ \sigma_m & \lambda_1 \leq \lambda \leq \lambda_2 \\ \sigma_m \frac{1-\lambda}{1-\lambda_2} & \lambda_2 \leq \lambda \leq 1 \end{cases} \quad (9)$$

where σ_m is the maximum stress in the cohesive element, and λ_1 and λ_2 are user defined boundary values between the three regimes.

The first regime ($\lambda \leq \lambda_1$) is analogous to the one defined in the elastic cohesive element presented in the previous section, with the stress growing linearly with the strain in the element. In the second regime ($\lambda_1 \leq \lambda \leq \lambda_2$) the traction plateaus as the cohesive element deforms, whilst in the third regime ($\lambda_2 \leq \lambda \leq 1$) the cohesive elements softens as the deformation increases until the complete (and irreversible) failure of the element when the traction is zero.

Finally, the traction is used to define the stress in the element as a function of the jump and the critical deformation in the tangential (δ_t^c) and normal (δ_n^c) directions;

$$\begin{Bmatrix} f_1 \\ f_2 \\ f_3 \end{Bmatrix} = \begin{bmatrix} \frac{t(\lambda)}{\lambda} \frac{\delta_n^c}{\delta_t^{c2}} & 0 & 0 \\ 0 & \frac{t(\lambda)}{\lambda} \frac{\delta_n^c}{\delta_t^{c2}} & 0 \\ 0 & 0 & \frac{t(\lambda)}{\lambda} \frac{1}{\delta_n^c} \end{bmatrix} \begin{Bmatrix} \delta_1 \\ \delta_2 \\ \delta_3 \end{Bmatrix}. \quad (10)$$

The adaptation of the TH cohesive formulation to the raster discretisation is more complex than the one implemented for the elastic formulation presented in the previous section, as the normal stress in the element local coordinates cannot be evaluated directly from the jump in the element local coordinate system.

First the deformation tensor is transformed using the rotation matrix \mathbf{N} , analogously to the elastic formulation;

$$\begin{Bmatrix} \delta_1 \\ \delta_2 \\ \delta_3 \end{Bmatrix} = \begin{bmatrix} N_y & N_z & N_x \\ N_z & N_x & N_y \\ N_x & N_y & N_z \end{bmatrix} \begin{Bmatrix} \delta_x \\ \delta_y \\ \delta_z \end{Bmatrix}. \quad (11)$$

The separation measure λ , the traction across the cohesive element $t(\lambda)$, and the stress components in the planar local coordinate system are then calculated using Eqs. (8)–(10), respectively.

Since the failure is modelled as the gradual reduction of the stiffness, which can happen at different rates along the tangential and normal direction with respect to the inclined plane, the transformation of the stress tensor from the [123] to $[\xi\eta\zeta]$ coordinate system is required to correctly calculate the stress in the raster element. The transformation of the stress is performed using the rotation matrix \mathbf{R} , calculated as the adjugate of \mathbf{N} used to rotate the strain components from the $[xyz]$ to [123] coordinate system;

$$\mathbf{R} = \begin{bmatrix} N_x N_z - N_y^2 & N_x N_y - N_z^2 & N_y N_z - N_x^2 \\ N_x N_y - N_z^2 & N_y N_z - N_x^2 & N_x N_z - N_y^2 \\ N_y N_z - N_x^2 & N_x N_z - N_y^2 & N_x N_y - N_z^2 \end{bmatrix}. \quad (12)$$

Consistent with the overall approach that allows raster cohesive elements to carry only normal stress (thus requiring three perpendicular raster elements to fully describe the response of an arbitrarily inclined planar interface), the component of the stress in the direction ζ is calculated using \mathbf{R}_ζ ,

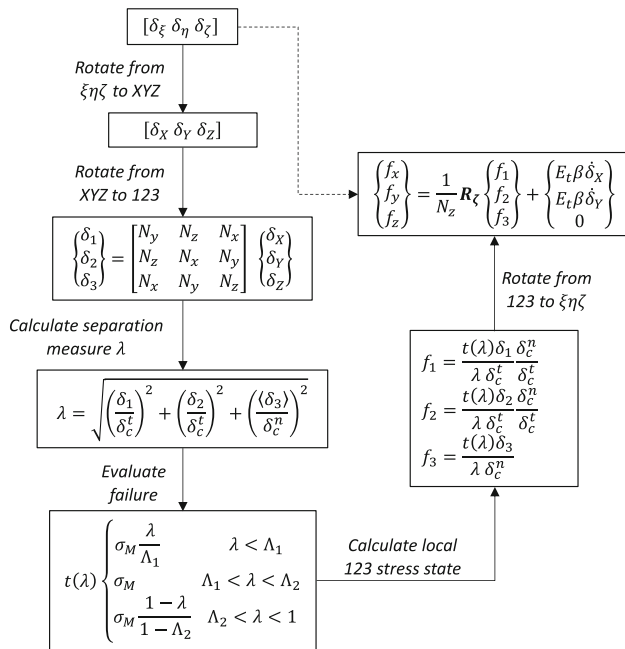


Fig. 5 Flowchart of the raster formulation of TH cohesive law

defined as a subset of the rotation matrix introduced in Eq. (12). Specifically, \mathbf{R}_ζ transforms the components of the stress in the [123] coordinate system into the component in the ζ direction. The first two rows of the matrix are equal to zero, and the last row is equal to the corresponding row in \mathbf{R} (i.e. first row if ζ is parallel to x , second row if ζ is parallel to y and third row if ζ is parallel to z). Additionally, a damping term is added to each component to reduce any possible vibration due to the lack of shear stiffness and the numerical error deriving from the rotation of the stress components. Thus we have,

$$\begin{Bmatrix} f_\xi \\ f_\eta \\ f_\zeta \end{Bmatrix} = \frac{1}{N_z} \mathbf{R}_\zeta \begin{Bmatrix} f_1 \\ f_2 \\ f_3 \end{Bmatrix} + \begin{Bmatrix} E_t \beta \dot{\delta}_\xi \\ E_t \beta \dot{\delta}_\eta \\ 0 \end{Bmatrix}, \quad (13)$$

where β is a user-defined damping factor, $\dot{\delta}$ the rate of deformation, and E_t the in-plane stiffness.

The algorithm to adapt the TH cohesive formulation to the raster approach is graphically described in the flowchart in Fig. 5.

4 Validation

To validate the presented cohesive law formulations, the deformation and failure of structures discretised whilst maintaining planarity of the interfaces is compared against the corresponding rasterised models.

First, a direct measure of the accuracy of both raster cohesive law formulations presented in this paper is provided by comparing the deformation and failure of bi-crystal models with a single arbitrarily inclined interface. Then, the scalability of the approach is proven by comparing the behaviour of FEM models of polycrystalline structures discretised with unstructured tetrahedral mesh against those using a structured raster discretisation.

4.1 Bi-crystal models

In this section three bi-crystal models are presented, consisting of a rectangular prism split by a single, arbitrarily inclined, planar interface. The simplicity of the chosen shapes enables easy discretisation of the geometries with structured meshes consisting of hexahedral elements, whilst still preserving the planarity of the interface. The models are compared against the raster discretisation of the same geometry, as presented in Fig. 6.

The direction cosines of the planar interfaces for each model are reported, alongside the orientation of the models with respect to the global [xyz] coordinate system. By analysing the response of models with longitudinal axes along three perpendicular directions, the validity of the full rotational matrices is verified.

The use of a structured mesh for both models minimises the possible influence of the element formulation over the final behaviour of the structure, as it avoids the use of tetrahedral or pentahedral elements (which can hinder the accuracy due to well-known integration issues), and limits distortion of the elements.

An isotropic elastic material model is assigned to the bulk elements (with Young's modulus $E = 400$ GPa), and a linearly increasing (tensile or compressive) displacement is applied to the two small external faces of the domain until the complete failure of the interface.

4.1.1 Elastic brittle

To validate the elastic-brittle cohesive law for raster elements, the three models presented in Fig. 6 are subjected to both tensile and compressive uniaxial loading conditions. In the models with a planar interface, the standard elastic-brittle material (known as MAT_184 in the commercial software LS-Dyna) is assigned to the cohesive elements, whilst the formulation described in Sect. 3.1 is imposed upon the cohesive elements in the rasterised models. The critical values of failure strength in mode I (f_n) and mode II (f_t) are both set equal to 1.0 GPa.

For the sake of conciseness, only the results of the simulations of Model 1 are presented in Fig. 7, showing excellent agreement between the model with planar interface and its rasterised counterpart. The results for Model 2 and 3 show

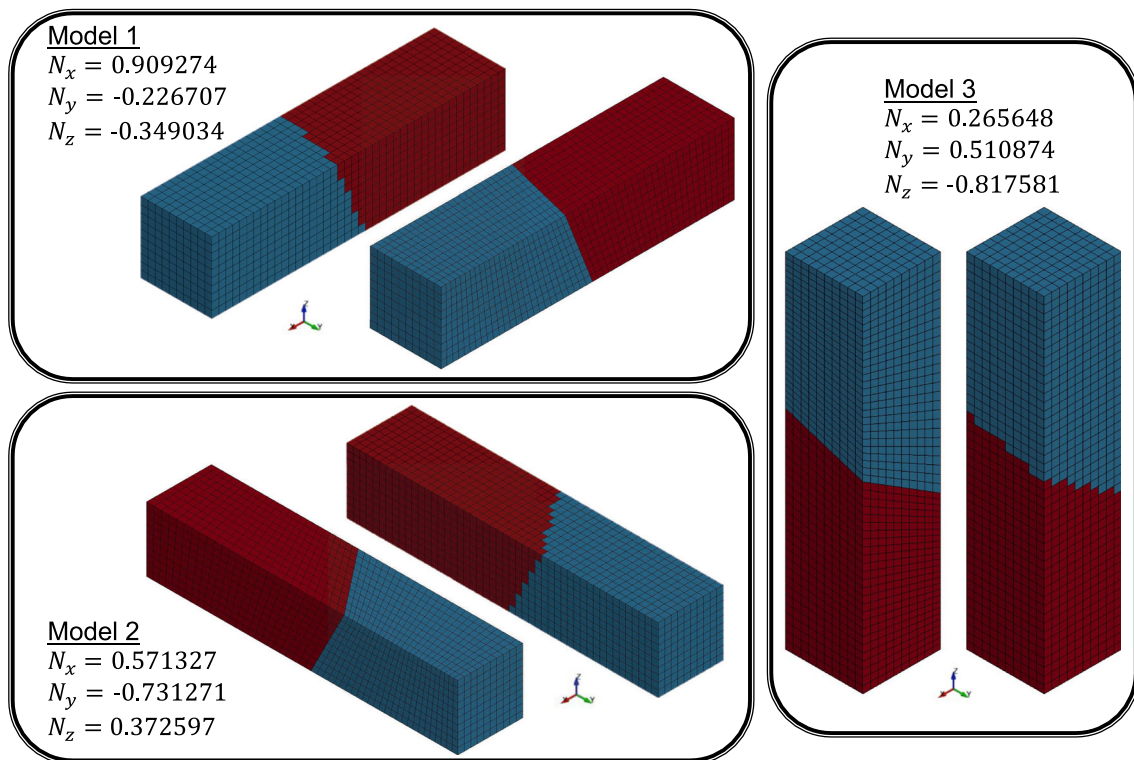


Fig. 6 Bi-crystal models used to compare the response of planar vs raster interfaces under tension and compression along the three principal axes. Uniaxial loads are applied along x for model 1, y for model 2, and z for model 3. Direction cosines $[N_x N_y N_z]$ of the planar interface are provided for each case

Table 1 MSPE between the bulk response of models with planar and raster elastic-brittle interfaces

	Tension (%)	Compression (%)
Model 1	0.0220	0.0083
Model 2	0.2384	0.0004
Model 3	0.1006	0.0032

a similar level of agreement, and are therefore not shown in the paper for sake of brevity. The maximum discrepancy between the planar and raster models is consistently within 1% for all components of stress. The mean square percentage error (MSPE) between the bulk response of models with planar and raster interfaces, summarised in Table 1, is within 0.25%, thus confirming the excellent agreement observed in the qualitative curve comparison.

Four components of the stress are compared: the stress in the bulk of the domain, the two shear components of the stress along the direction of the short edges of the domain (always assumed positive), and the component of stress normal to the planar interface, proving that the implemented cohesive law accurately reproduces the failure, both in tension and compression, of a planar boundary using a structured mesh with raster interface. The comparison shows also the ability

of the raster cohesive formulation to reproduce both mode I and mode II failure mechanisms, as the failure of the model under tension is due to $f_3 = f_n$, whilst the failure of the interface under compression is due to $\sqrt{f_1^2 + f_2^2} = f_t$.

Finally, even in the simple bi-crystal models presented it is possible to observe an already mentioned limitation of the simplistic elastic-brittle approach. The abrupt failure of the interface and consequent sudden release of energy in the system lead to the propagation of unphysical vibrations, as observed in the post-fracture behaviour of the bulk stress in models with raster and planar interface alike. The implementation of the more complex TH cohesive law limits this phenomenon, introducing a more physically based description of inter-granular crack propagation mechanisms.

4.1.2 Tvergaard–Hutchinson

An analogous validation process has been performed to validate the raster implementation of the TH formulation. The TH material model (defined as MAT_185 in LS-Dyna) is assigned to the cohesive elements in the models with planar interface presented in Fig. 6, whilst the raster formulation of TH cohesive law described in Sect. 3.2 is used for the interface elements of the rasterised models.

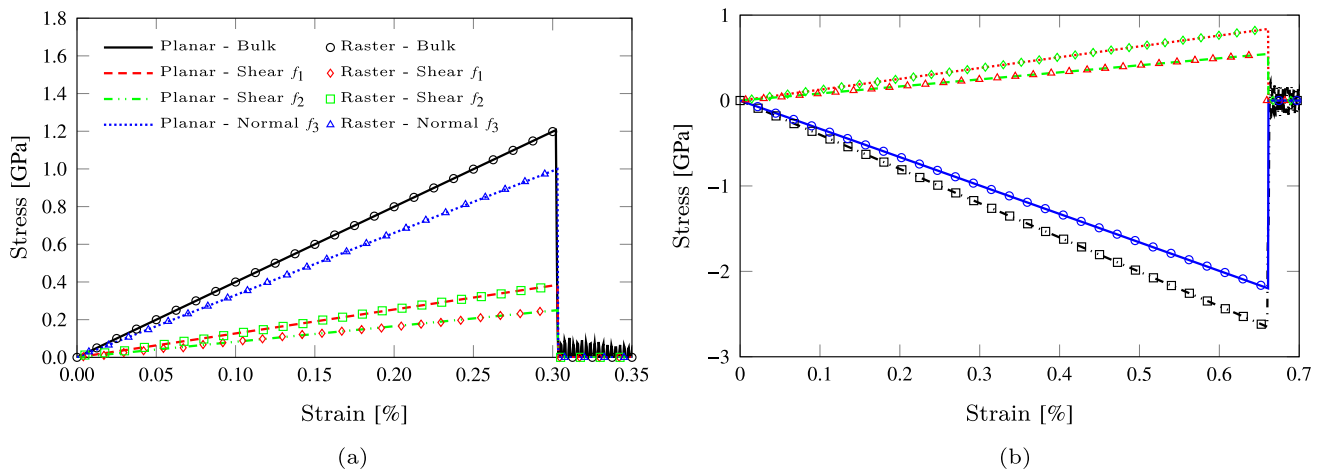


Fig. 7 Comparison of the stress components in the bulk and in the interface for Model 1 under uniaxial tension **(a)** and compression **(b)**

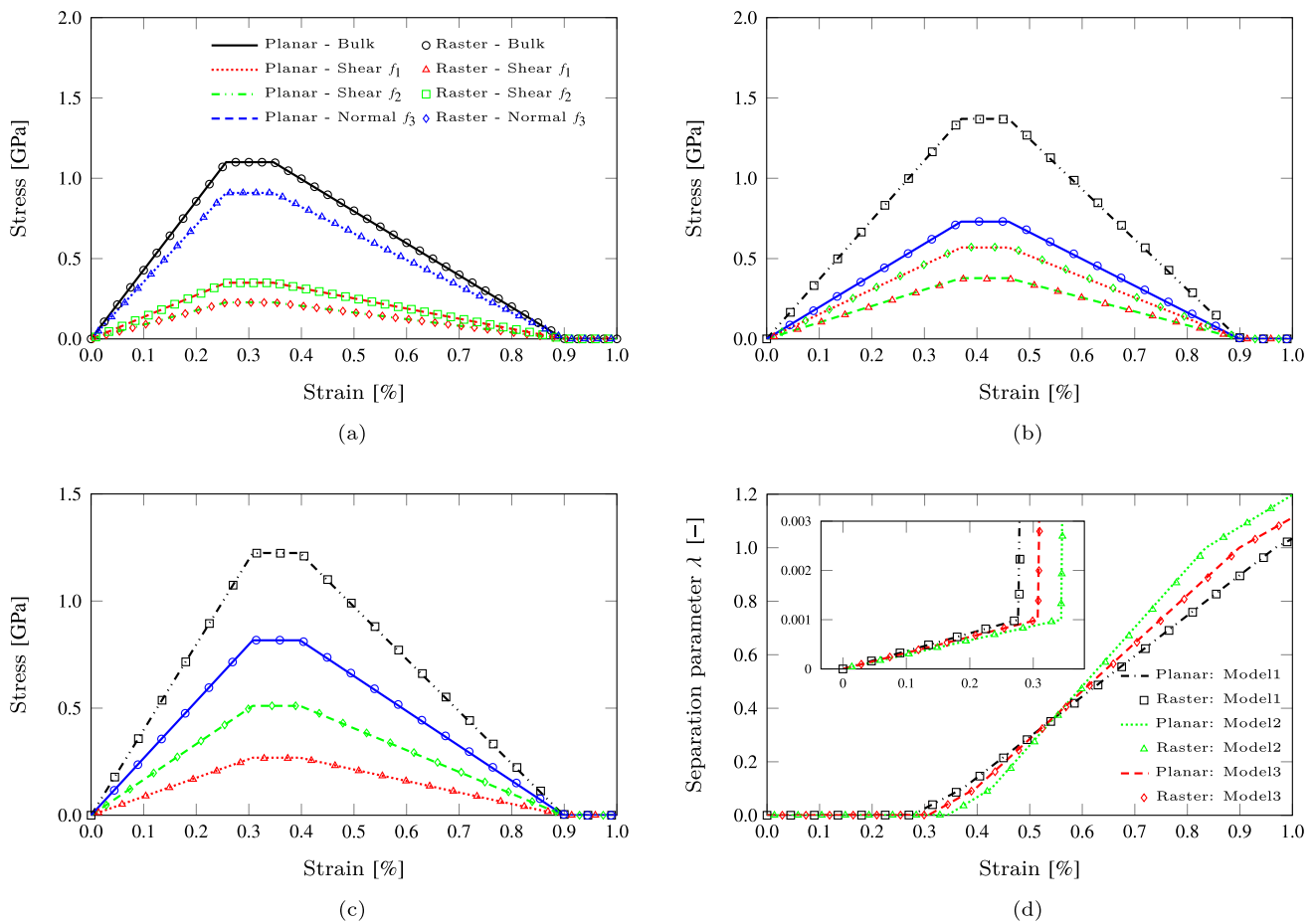


Fig. 8 Comparison of the stress components in the bulk and in the interface for **a** Model 1, **b** Model 2, and **c** Model 3 under uniaxial tension, alongside **d** the evolution of λ in all three models

The bulk material is still modelled as isotropic elastic (with Young's modulus $E = 400$ GPa), and the interfaces have the same maximum strength as for the elastic-brittle validation (i.e. $\sigma_M = 1.0$ GPa). The critical deformation in the normal (δ_n^c) and tangential (δ_t^c) direction are set equal to $20\mu\text{m}$, and the limits of the linear elastic (λ_1) and plateau (λ_2) regimes presented in Fig. 4 are imposed to be equal to 0.001 and 0.1, respectively, which is equivalent to a value of energy release rate of approximately $G_{Ic} \approx 11\text{kJm}^{-2}$. The properties are not representative of any specific material, as they were chosen to highlight the consistency of all three regimes of the CZM formulation. However they are not entirely unphysical; the energy release rate is consistent with that of relatively brittle flavours of Titanium alloys [24].

The comparison of the behaviour of the models under uniaxial tensile loading conditions is presented in Fig. 8. The results, visualised in terms of stress along the loading direction measured in the bulk of the model, shear components of the cohesive elements stress along the edges of the planar interface, and component of the cohesive elements stress normal to the planar interface for the three models presented in Fig. 6, show excellent agreement for all the stress components. Furthermore the evolution of the separation parameter λ extracted from the rasterised models is practically identical to the one measured from the models discretised with planar interface. The only difference between the models is a systematic discrepancy in terms of opening gap, which is proportional to the direction cosines, due to the difference in surface areas between the raster and the planar surfaces. For relatively brittle materials the effect of the approximation is negligible, but it might affect the accuracy of the simulation of the behaviour of very ductile interfaces (e.g. deformable adhesives). The modification of the element formulation to increase the accuracy of the calculation of δ for tough materials requires the implementation of a novel element formulation combined with the novel CZM presented in this paper. The development and implementation of the novel cohesive element formulation will be the topic of future work.

Finally, it is important to highlight the absence of unphysical vibrations in the bulk elements after failure, proving that the TH cohesive formulation overcomes the limitation shown by the simplistic elastic-brittle cohesive formulation.

4.2 Polycrystalline models

To verify the capability to model the behaviour of multiple interfaces, a polycrystalline structure, consisting of 21 grains, has been generated using the approach described in Sect. 2.1. The structure is discretised with an unstructured tetrahedral mesh, which allows for preservation of the planarity of the grain boundaries; and with a structured hexahedral mesh, as presented in Fig. 9.

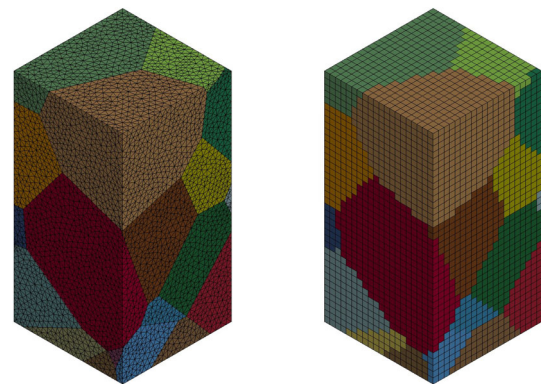


Fig. 9 Unstructured (left) and structured (right) discretisation of the polycrystalline structure consisting of 21 grains

A fully anisotropic elastic material model is imposed upon the bulk elements, with different crystallographic orientations assigned to each grain. The aim is to prove the compatibility of the raster formulation with more complex constitutive models than the simple isotropic elastic relation used for the bi-crystal verification models. The material properties of alumina, as measured by Hovis [25], are used in the simulations presented in this paper.

In the model discretised with an unstructured mesh, traditional cohesive elements are inserted along the planar interfaces between grains, whilst the raster formulation is adopted for the interfaces of the model consisting of hexahedral elements. The same properties applied to the cohesive elements in the bi-crystal models are adopted, with maximum strength of 1.0 GPa for both formulations and toughness $G_{Ic} \approx 11\text{Jm}^{-2}$ for the TH formulation.

The models are subjected to uniform tensile stress by imposing linearly increasing displacement to the top and bottom faces of the models.

First the elastic-brittle TSL (presented in Sect. 3.1) is assigned to the cohesive elements. The comparison of the normal stress contour ahead of failure presented in Fig. 10, shows the ability of the raster approach to reproduce the stress state of the equivalent planar interface even within a complex model with multiple interconnected interfaces, whilst avoiding the occurrence of unphysical high values of stress concentrations due to the presence of distorted elements that can be observed in the unstructured model. Additionally, the combination of high computational efficiency of the structured mesh and absence of small or distorted elements leads to a reduction of run-time required for the simulation of several orders of magnitude. Specifically, the simulations presented in Fig. 10 were performed using 16 SMP on a machine equipped with 2 8-core/16-thread processors (Xeon E5-2640 at 2.60 GHz) and 64 GB of RAM, and it took 92 s for the rasterised model to reach the complete failure of the structure, several times faster than the same simulation using

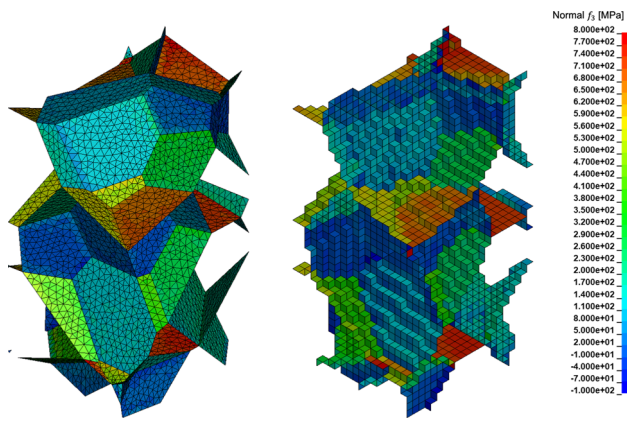


Fig. 10 Comparison of the normal stress contour plot on the interfaces of the polycrystalline models with unstructured (left) and structured (right) meshes

the model with planar grain boundaries, which took more than 6 h on the same machine.

The same polycrystalline models presented in Fig. 9 are also used to validate the raster formulation of Tvergaard–Hutchinson TSL (described in Sect. 3.2). The same bulk material properties and loading conditions used for the elastic-brittle validation are applied to the model, whilst the standard and raster TH cohesive elements are inserted along the grain boundaries of the models.

As for the elastic-brittle models, the raster formulation is able to reproduce the deformation and failure of the structure, as shown in Fig. 11. The curves, representing the nominal stress evaluated as the total force measured on the top and bottom faces of the model over the initial cross sectional area, show good agreement between the planar and raster interface approach. The slight difference (less than 5% at any strain) observed in the evolution of the curves is comparable to the mismatch between the stress evaluated from the top and bottom faces of the same model, and considered to be due to the anisotropic nature of the grains combined with stress localisations introduced by the irregular discretisation of the unstructured mesh.

Also for the TH formulation, the use of the rasterised model leads to a significant reduction of the duration of the simulation. Specifically, the model consisting of planar interfaces ran for more than 30 h until the complete failure of the model, whilst the equivalent rasterised model took just over 3 h to reach the same condition.

5 Micromechanical models

To prove the scalability and the computational efficiency of the cohesive element formulations presented in this paper, micromechanical simulations have been setup to model the

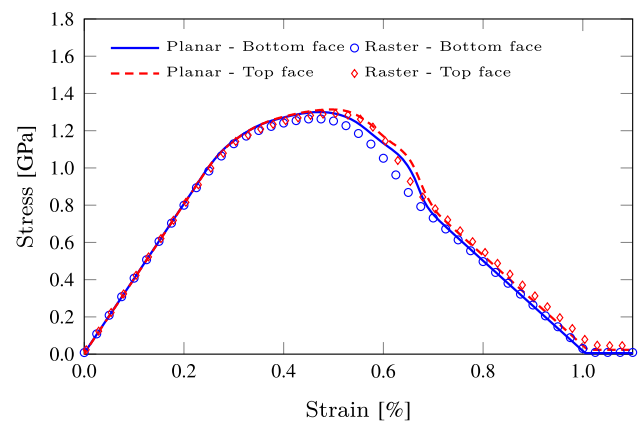


Fig. 11 Comparison of the nominal stress evaluated from the total forces measured on the bottom and top faces of the *raster* and *planar* models

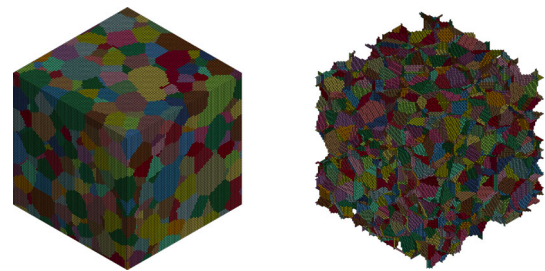


Fig. 12 Raster discretisation of the bulk (left) and the grain boundaries (right) of the synthetic microstructure

initiation and propagation of inter-granular failure within relatively large polycrystalline microstructures.

A synthetic microstructure of 0.2 mm per side is generated, consisting of 754 grains and with a realistic distribution of grain sizes ($6\mu\text{m} < d < 50\mu\text{m}$), as illustrated in Fig. 12.

The structure is discretised using the raster approach described in Sect. 2.2, producing a structured mesh consisting of 512k bulk elements and over 185k zero-thickness cohesive elements. The grains are modelled as anisotropic elastic crystals, and either the elastic-brittle or the TH cohesive formulations are assigned to the interfaces. Realistic material properties are used to model the single crystals and the grain boundaries based on the properties of a relatively brittle flavour of zirconium [26]. Specifically the full anisotropic compliance tensor \mathbf{C} reported in Eq. (14) is assigned to the single crystals alongside randomly oriented crystallographic texture.

$$\mathbf{C} = \begin{bmatrix} 152.4 & 65.5 & 66.6 & 0.0 & 0.0 & 0.0 \\ & 152.4 & 66.6 & 0.0 & 0.0 & 0.0 \\ & & 173.8 & 0.0 & 0.0 & 0.0 \\ & & & 24.6 & 0.0 & 0.0 \\ \text{sym} & & & & 24.6 & 0.0 \\ & & & & & 43.5 \end{bmatrix} \text{ GPa}. \quad (14)$$

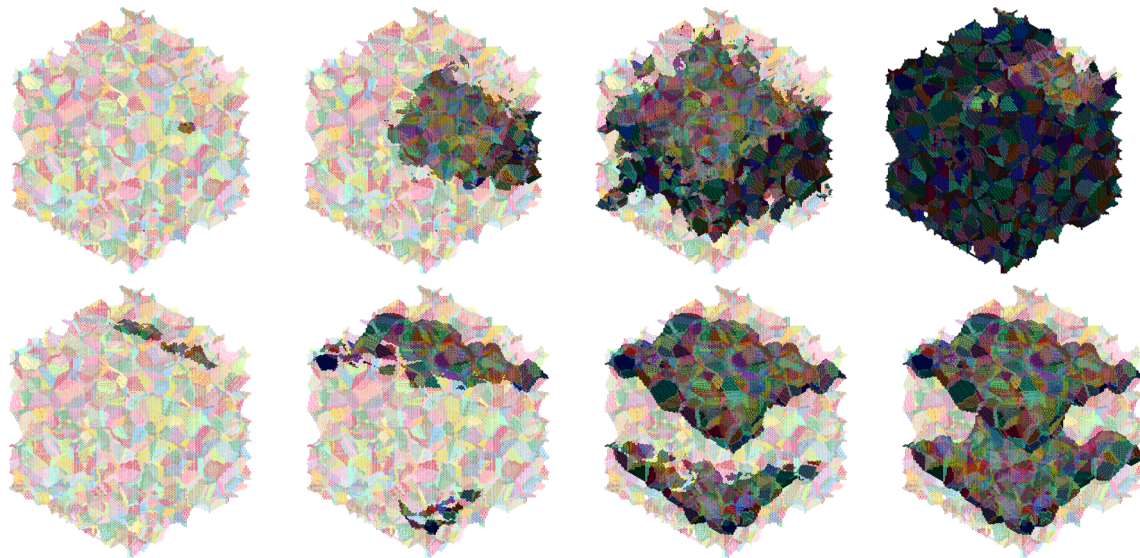


Fig. 13 Evolution of inter-granular failure within a polycrystalline microstructure with interface modelled with either the elastic-brittle (top) or the TH (bottom) cohesive element formulation

Critical failure stress of 200 MPa is assigned to the grain boundaries for both elastic-brittle and TH cohesive formulations. Critical deformations (δ_n^c) and (δ_t^c) are both equal to $1\text{ }\mu\text{m}$ and the elastic behaviour limit (λ_1) equal to 0.001 for the triangular (i.e. $\lambda_1 = \lambda_2$) TH cohesive formulation, which is equivalent to a value of energy release rate $G_c \approx 0.1\text{ kJ/m}^2$ which is consistent with directly measured values for brittle grain boundaries [27].

Displacement controlled uniaxial loading conditions are applied to the top and bottom faces of the models at a rate of 0.1 mm/ms until the complete failure of the structure. The outcome of the simulations is reported graphically in Fig. 13. The top row shows the evolution of failed interfaces modelled using the elastic-brittle cohesive formulation, whilst the bottom row shows the failure of the same microstructure with grain boundaries modelled using the TH cohesive formulation.

The behaviour of the large models is consistent with what was observed for the polycrystalline validation presented in Sect. 4.2, with interface failure initiating at the boundary between grains with highest crystallographic mismatch and propagating along grain boundaries until the complete failure of the structure. The simulations also show the advantage of the TH cohesive formulation which provides a more realistic inter-granular crack pattern, with the relatively slow initial growth of a first crack causing the volume around the crack to relax (often referred to as crack shadowing). The corresponding stress increase in the not-relaxed volume of the RVE leads, in turn, to the initiation of a second crack. The two cracks evolve separately along grain boundaries with a limited amount of branching until the complete failure of the domain split into three fragments. The simulated behaviour

is markedly different from the failure observed in almost all grain boundaries modelled with the elastic-brittle cohesive elements, avoiding any abrupt, unphysical releases of energy upon deletion of elements.

The numerical results highlight the already mentioned limitations of the elastic-brittle formulation, with the abrupt loss of strength in cohesive elements triggering the failure of neighbour elements until unphysical complete failure of nearly all the grain boundaries.

The computational efficiency of the cohesive element formulations scales well to large models, with the simulations taking over 3 h and almost 28 h for the elastic-brittle and the TH cohesive formulation respectively, using 16 SMP on a machine equipped with 2 8-core/16-thread processors (Xeon E5-2640 at 2.60 GHz) and 64 GB of RAM. The relatively small simulation times for such large models prove the high computational efficiency of the two configurations. It is important to highlight that the complete failure of the model with elastic-brittle cohesive elements occurs shortly after the initiation of the first crack, whilst the onset of the first crack for the TH formulation occurs after 19 h of simulation as the crack growth is significantly slower allowing for the stress redistribution within the model as the crack pattern evolves.

6 Conclusions

The paper presents the formulation and implementation of a cohesive model approach capable of reproducing the failure of arbitrarily inclined interfaces using structured meshes consisting of highly regular hexahedral elements.

The approach presented relies on the newly implemented capability of the algorithm VorTeX (developed by the authors) to impose a raster discretisation of complex polycrystalline structures, maintaining the information on the grain boundary inclination in the three-dimensional space. By linking the actual orientation of the grain boundary normal with the cohesive elements inserted in the raster discretisation, the novel formulation presented is able to reproduce the behaviour of cohesive elements inserted on the actual inclined interface.

The approach developed is applied to two cohesive models: elastic-brittle and Tvergaard–Hutchinson material models.

The independence of the stiffness value from the deformation state in the elastic-brittle formulation allows the decoupling of the calculation of the stress state in the element and the verification of failure conditions, thus increasing the computational efficiency by avoiding stress transformation from local to global coordinate system. However, the relatively simplistic nature of the elastic-brittle formulation leads to abrupt energy release in the system at failure, which can trigger unphysical failure of neighbouring elements and affect the accuracy of the simulation.

The TH cohesive model overcomes this limitation by introducing 3 stiffness regimes linked to the deformation state. The adaptation of the TH model for raster mesh application does not allow for a decoupling of the evaluation of the stress state and the failure condition, as it requires the transformation of the stress state from local to global coordinates. However, the increase in computational cost for the single cohesive element is more than compensated by the increase in computational efficiency due to use of a highly regular structured mesh. For example, simulation to failure of the same polycrystalline microstructure takes less than 2 min with the raster approach versus 6 h for the unstructured model. This significant increase in computational efficiency for raster models is primarily due to the absence of any small or distorted elements in structured meshes.

In addition to a reduction in simulation run-time, the use of raster cohesive elements permits the full automation of the meshing process as presented in [20], therefore virtually eliminating time-consuming and labour-intensive discretisation of complex structures.

The validations presented in the paper show excellent agreement between the raster and standard formulations, both in the one-to-one comparison of the elements and in the behaviour of complex structures, proving the raster approach developed to be an effective alternative to the standard cohesive elements for polycrystalline structures, or more generalised domains incorporating irregular and intersecting interfaces.

Finally, the failure of large polycrystalline structures is modelled using the two cohesive element formulations pre-

sented in this paper, proving the scalability of the presented algorithms to large models and their ability to reproduce realistic inter-granular failure patterns.

Acknowledgements The authors gratefully acknowledge the support of the United Kingdom Defence Science and Technology Laboratory (DSTL), Grant No: DFR05710.

Open Access This article is licensed under a Creative Commons Attribution 4.0 International License, which permits use, sharing, adaptation, distribution and reproduction in any medium or format, as long as you give appropriate credit to the original author(s) and the source, provide a link to the Creative Commons licence, and indicate if changes were made. The images or other third party material in this article are included in the article's Creative Commons licence, unless indicated otherwise in a credit line to the material. If material is not included in the article's Creative Commons licence and your intended use is not permitted by statutory regulation or exceeds the permitted use, you will need to obtain permission directly from the copyright holder. To view a copy of this licence, visit <http://creativecommons.org/licenses/by/4.0/>.

References

1. Song J-H, Wang H, Belytschko T (2008) A comparative study on finite element methods for dynamic fracture. *Comput Mech* 42(2):239–250
2. Pandolfi A, Ortiz M (2012) An eigenerosion approach to brittle fracture. *Int J Numer Methods Eng* 92(8):694–714
3. Moës N, Belytschko T (2002) Extended finite element method for cohesive crack growth. *Eng Fract Mech* 69(7):813–833
4. Randles P, Libersky LD (1996) Smoothed particle hydrodynamics: some recent improvements and applications. *Comput Methods Appl Mech Eng* 139(1–4):375–408
5. Barbieri E, Petrinic N (2014) Three-dimensional crack propagation with distance-based discontinuous kernels in meshfree methods. *Comput Mech* 53(2):325–342
6. Rabczuk T (2013) Computational methods for fracture in brittle and quasi-brittle solids: state-of-the-art review and future perspectives. *Int Schol Res Not* 2013:1–38
7. Radovitzky R, Seagraves A, Tupek M, Noels L (2011) A scalable 3D fracture and fragmentation algorithm based on a hybrid, discontinuous Galerkin, cohesive element method. *Comput Methods Appl Mech Eng* 200(1–4):326–344
8. Ortiz M, Suresh S (1993) Statistical properties of residual stresses and intergranular fracture in ceramic materials. *J Appl Mech* 60:77
9. Xu X-P, Needleman A (1994) Numerical simulations of fast crack growth in brittle solids. *J Mech Phys Solids* 42(9):1397–1434
10. Zhang Z, Paulino GH, Celes W (2007) Extrinsic cohesive modelling of dynamic fracture and microbranching instability in brittle materials. *Int J Numer Methods Eng* 72(8):893–923
11. Camacho GT, Ortiz M (1996) Computational modelling of impact damage in brittle materials. *Int J Solids Struct* 33(20–22):2899–2938
12. Ortiz M, Pandolfi A (1999) Finite-deformation irreversible cohesive elements for three-dimensional crack-propagation analysis. *Int J Numer Methods Eng* 44(9):1267–1282
13. Pandolfi A, Ortiz M (1998) Solid modeling aspects of three-dimensional fragmentation. *Eng Comput* 14(4):287–308
14. Zienkiewicz OC, Taylor RL, Zhu JZ (2005) The finite element method: its basis and fundamentals. Elsevier
15. CAE Altair HyperWorks: Hypermesh. <https://altairhyperworks.com/product/HyperMesh>

16. Blacker TD, Bohnhoff WJ, Edwards TL (1994) Cubit mesh generation environment. Volume 1: users manual. Technical report, Sandia National Labs., Albuquerque
17. Heilig G, Durr N, Sauer M, Klomfass A (2013) Mesoscale analysis of sintered metals fragmentation under explosive and subsequent impact loading. *Proced Eng* 58:653–662
18. Feather WG, Lim H, Knezevic M (2021) A numerical study into element type and mesh resolution for crystal plasticity finite element modeling of explicit grain structures. *Comput Mech* 67(1):33–55
19. Lee M-J, Jeon Y-J, Son G-E, Sung S, Kim J-Y, Han HN, Cho SG, Jung S-H, Lee S (2018) Grain boundary conformed volumetric mesh generation from a three-dimensional voxellated polycrystalline microstructure. *Met Mater Int* 24(4):845–859
20. Falco S, Fogell N, Kasinos S, Iannucci L (2022) Homogenisation of micromechanical modelling results for the evaluation of macroscopic material properties of brittle ceramics. *Int J Mech Sci* 220:107071
21. Falco S, Bombace N, Brown P, Petrinic N (2019) Implementation of a method for the generation of representative models of polycrystalline microstructures in ls-prepost. In: 12th European LS-DYNA users conference
22. Falco S, Jiang J, De Cola F, Petrinic N (2017) Generation of 3d polycrystalline microstructures with a conditioned Laguerre–Yoroi tessellation technique. *Comput Mater Sci* 136:20–28
23. Tvergaard V, Hutchinson JW (1996) Effect of strain-dependent cohesive zone model on predictions of crack growth resistance. *Int J Solids Struct* 33(20–22):3297–3308
24. Richards N (2004) Quantitative evaluation of fracture toughness-microstructural relationships in alpha-beta titanium alloys. *J Mater Eng Perform* 13:218–225
25. Hovis D, Reddy A, Heuer A (2006) X-ray elastic constants for α - Al_2O_3 . *Appl Phys Lett* 88:131910–1319103
26. Weck PF, Kim E, Tikare V, Mitchell JA (2015) Mechanical properties of zirconium alloys and zirconium hydrides predicted from density functional perturbation theory. *Dalton Trans* 44(43):18769–18779
27. Norton A, Falco S, Young N, Severs J, Todd R (2015) Micro-cantilever investigation of fracture toughness and subcritical crack growth on the scale of the microstructure in Al_2O_3 . *J Eur Ceram Soc* 35(16):4521–4533

Publisher's Note Springer Nature remains neutral with regard to jurisdictional claims in published maps and institutional affiliations.